Politecnico di Torino

Politecnico di Torino

PHYSICS OF COMPLEX SYSTEMS

A.a. 2024/2025

Sessione di laurea July 2025

Mechanics of a Lipid Membrane Coupled to a Transmembrane Protein: A Theoretical and Numerical Study

Relatori:

Michele Castellana

Andrea Gamba

Candidati:

Gaetano Ferraro

Indice

Introduction

The interaction between cell membranes and proteins plays a central role in many biological processes, from signaling to morphogenesis. A widely used modeling approach treats membrane-associated proteins as point-like entities that exert localized forces and torques on the membrane. This simplification enables analytical calculations but neglects structural details that may become important at small, but finite, length scales.

The aim of this thesis is to study how the finite size and anchoring geometry of transmembrane proteins affect membrane deformation and force transmission, beyond what is captured by point-force models.

The thesis is structured in two main parts. In the first part, we investigate the static deformation of the membrane due to a single protein that imposes a prescribed anchoring angle and a certain displacement of the membrane's boundary. After deriving the membrane shape numerically and comparing it with analytical solutions, we analyze the force exerted by the membrane on the protein in different conditions.
While similar problems have been studied in the literature (notably in [1]), our analysis extends the classical framework by considering proteins with finite size and anchoring angles, as well as different types of external boundary conditions. At the end of the first part, we quantify the interaction between two membrane inclusions as a function of their distance.
In the second part of the thesis, we study the dynamical coupling between membrane deformation and lipid flow in the presence of a finite-size protein. In this context, the governing equations simplify under certain assumptions, allowing us to identify an instability mechanism that emerges from the interplay between curvature and flow. Finally, we compute the viscous forces exerted on the protein by the flowing membrane and compare our numerical results with existing theoretical predictions.

Through this study, we aim to provide a more complete picture of protein–membrane interaction by incorporating finite-size effects and dynamical couplings that are often overlooked in the literature.

Capitolo 1

Physical model

1.1 General Comments on the Model

This work focuses on describing the interaction between the cellular membrane and a transmembrane protein from a coarse-grained perspective, disregarding the microscopic and discrete nature of the membrane.
The membrane is modeled as a two-dimensional smooth manifold embedded in the three-dimensional space, represented by the mapping:

$$\sigma : \mathbb{R}^2 \to \mathbb{R}^3 \tag{1.1}$$

The presence of the protein is modeled through well-defined boundary conditions imposed at the interface between the protein and the membrane. The flow of phospholipids is incorporated by introducing a velocity field defined at each point on the membrane. This velocity vector is decomposed into tangential and normal components, namely:

$$\vec{v} = v^i \vec{e_i} + w\hat{n} \tag{1.2}$$

where $\vec{e_i}$ are the local tangent basis vectors and $\vec{n}$ is the normal vector (appendix 4.3.1).

The dynamics of the system is governed by three fundamental equations:

- Conservation of mass;
- Conservation of momentum;
- Evolution equation for the membrane's shape.

The full equations (derivation based on [2][3]) are presented in the next section, even if just a simplified version of them is going to be used.

1.2 Validity of the model

The model considered in this work is based on a continuum, coarse-grained description of the lipid membrane and protein interactions. While this framework captures the large-scale mechanical and geometric features of the membrane, it involves several approximations that limit its range of validity:

- The model assumes that the membrane behaves as a smooth two-dimensional surface embedded in a three-dimensional space. This description breaks down when deformations occur at length scales comparable to the thickness of the lipid bilayer (typically a few nanometers). At such small scales, the discrete molecular structure of the membrane and the individual behavior of lipid molecules cannot be neglected, and atomistic or molecular dynamics models become necessary.

- Thermal fluctuations are neglected, just the minimum of the energy is considered. In regimes where fluctuation-induced effects (such as entropic forces or fluctuation-stabilized structures) are significant, the deterministic treatment of the membrane shape and protein fields becomes insufficient. A fully stochastic or statistical mechanical treatment may be required to accurately capture the behavior in those cases.

Therefore, the model remains valid primarily in the regime of large-scale, smooth deformations (typically above tens of nanometers), where the membrane behaves as a viscoelastic medium and thermal fluctuations do not dominate the physics. Outside this regime, more detailed models (molecular or stochastic) are necessary to obtain reliable predictions.

1.3 Governing Equations

The equation for the conservation of mass can be obtained from the conservation law for a scalar quantity defined on a 2D deformable surface (see the

appendix **??**):

$$\frac{\partial \rho}{\partial t} + \nabla_i(\rho v^i) - 2\rho w H = 0 \tag{1.3}$$

where H is the mean curvature.
This equation states that changes in the surface density ρ arise both from the in-surface flow (encoded in $\nabla_i(\rho v^i)$) and from changes in the local surface area due to the membrane's normal velocity, captured by the term wH.

Since we assume that the phospholipid fluid is incompressible, the surface density ρ is constant. Therefore, the equation simplifies to:

$$\nabla_i v^i - 2wH = 0 \tag{1.4}$$

This implies that a converging tangential flow (i.e., $\nabla_i v^i < 0$) is associated with a local outward deformation (positive w), and vice versa.

1.3.1 Conservation of momentum

The equation for momentum conservation can be derived from the general conservation law applied to a vector field. Since momentum is a three-dimensional vector, each component must be conserved independently[1].

The general form of the momentum conservation equation is:

$$\frac{\partial v^\gamma}{\partial t} + \nabla_i(v^\gamma v^i) - v^\gamma w H = b^\gamma + \operatorname{div} \vec{b^\gamma} \tag{1.5}$$

This equation states that the variation of the γ-th component of momentum is due to body forces b^γ (e.g., due to interactions with the environment) and to momentum exchange across the surface, described by the divergence of the stress vector field $\vec{b^\gamma}$.

The decomposition of Eq. (1.5) into tangential and normal components can be performed by expressing the momentum vector as:

$$\rho \vec{v} = \rho v^i \vec{e}_i + \rho w \hat{n} \tag{1.6}$$

where $\vec{e^i}$ denotes the local tangent basis vectors of the surface (defined in Appendix 4.3.1).

[1]The conservation of momentum cannot be derived directly for the tangential components alone, as momentum at different points can only be compared in the embedding space $\mathbb{R}^3$.

The full momentum conservation equation (1.5) is then projected along the tangential and normal directions using the dual basis vectors. The projection yields three equations governing the in-surface (tangential) and out-of-plane (normal) dynamics of the membrane.

In this work, bulk forces due to the surrounding fluid are neglected.
For tangential components, this is justified by the fact that the viscosity of the surrounding fluid is much smaller than that of the membrane.
For normal components, the assumption works because we consider stationary configurations and the external fluid inertia is negligible when $w = 0$ (stationary conditions).

1.3.2 Full equations

The final equations are [4]:

$$\begin{cases} \nabla_i v^i - 2Hw = 0, \\ \rho\left(\partial_t v^i + v^j \nabla_j v^i - 2v^j w b^i_j - w\nabla^i w\right) = \\ \nabla^i \sigma + \eta\left[-(\Delta_{LB} v)^i - 2(b^{ij} - 2Hg^{ij})\nabla_j w + 2Kv^i\right], \\ \rho\left[\partial_t w + v^i\left(v^j b_{ij} + \nabla_i w\right)\right] = \\ 2\kappa\left[\nabla^i\nabla_i H - 2H(H^2 - K)\right] + 2H\sigma + \\ +2\eta\left[b_{ij}\nabla^i v^j - 2w(2H^2 - K)\right], \\ \partial_t z = w\left[(\hat{n})^3 - (\hat{n})^i \partial_i z\right] \end{cases}$$

Where the values of the physical quantities appearing in the equations are in table 1.1, (values taken from [4, 5, 6]).
It is convenient to non-dimensionalize the equations. This approach is useful to identify the relevant dimensionless parameters and to work with quantities whose order of magnitude is near unity.
The chosen characteristic scales are:

- **Characteristic length scale**: the size of the protein, denoted by r_0;
- **Characteristic velocity**: the velocity of the protein v_{th}, or equivalently, the velocity of the flow far from the protein in the reference frame where the protein is at rest.

Physical parameter	**SI**	**Optimal units**
$\mathtt{l}$ (dimension of the protein)	10^{-8} m	$1\ r_0$
$\eta_{3\mathtt{D}}$ (3D viscosity)	1 N m^{-2}s	-
$\eta_{2\mathtt{D}}$ (2D viscosity)	-	0.1 pN r_0^{-1} ms
σ (line tension)	$10^{-6} - 10^{-8}$ N m^{-1}	$10^{-2} - 10^{-4}$ pN r_0^{-1}
κ (bending rigidity)	3×10^{-20} N m	3 pN r_0
v_{th} (typ. thermal velocity)	10^{-5} m s^{-1}	1 r_0 ms^{-1}
$\rho_{2\mathtt{D}}$ (2D membrane density)	-	5×10^{-12} pN r_0^{-3} ms^2

Tabella 1.1: Values of the parameters for cellular membranes. The values are expressed in the SI and in a system of unit choosen to have numbers of the of unity.

After non-dimensionalization, the equations take the form:

$$\begin{cases} \nabla_i v^i - 2Hw = 0, \\ \mathrm{Re}\left(\partial_t v^i + v^j \nabla_j v^i - 2v^j w b^i_j - w\nabla^i w\right) = \\ \mathrm{Re}\nabla^i \sigma + \left[-(\Delta_{LB} v)^i - 2(b^{ij} - 2Hg^{ij})\nabla_j w + 2Kv^i\right], \\ \mathrm{Re}\left[\partial_t w + v^i\left(v^j b_{ij} + \nabla_i w\right)\right] = \\ 2\mathrm{A}\left[\nabla^i \nabla_i H + 2H(H^2 - K)\right] + 2\sigma \mathrm{Re}H + \\ +2\left[b_{ij}\nabla^i v^j - 2w(2H^2 - K)\right], \\ \partial_t z = w\left(\hat{n}\hat{z} - (\hat{n})^i \partial_i z\right) \end{cases}$$

As can be seen, two non-dimensional parameters determine different regimes of the system, these are:

- $\mathrm{Re} = \frac{\rho v_{th} r_0}{\eta}$, that is the Reynold's number that in the case under study is really small $\mathrm{Re} \simeq 5 \times 10^{-11}$. This dimensionless number describes the ratio between variation in momentum density due to transport of momentum and shear stresses.
- $\mathrm{A} = \frac{\kappa}{v_{th}\eta r_0}$, that is, a dimensionless parameter that describes the ratio between the variation in momentum density due to elastic stresses and shear stresses. The value of this parameter is $\mathrm{A} \simeq 10$.

The fact that $\mathrm{Re} \ll 1$ will be used in the following to simplify the equations.

Capitolo 2

Finite element method

Given the high nonlinearity of the governing equations, numerical methods have been implemented to gain insight into the system and to provide support for analytical estimates. In particular, the finite element method (FEM) has been employed, that is, a powerful numerical technique that allows to handle complex systems of coupled partial differential equations (PDEs). This approach enables the evaluation of the membrane shape (see figure **??**) as well as physical quantities such as the total energy, stress distributions, boundary forces, and other relevant observables.
The core idea behind FEM is to approximate the solution of a partial differential equation by projecting it onto a finite-dimensional function space, thereby transforming the continuous problem into a system of discrete algebraic equations for the linear coefficient of the Fourier decomposition of the solution. The accuracy of the numerical solution depends on how well the chosen function space can represent the true solution. The richer the approximation space, the smaller the error with respect to the exact solution. Once a suitable set of basis functions for the finite-dimensional space is selected, denoted $\{\psi_n(\vec{r})\}_n$, the approximate solution is written as:

$$\psi^*(\vec{r}) = \sum_n a_n \psi_n(\vec{r}),$$

where the coefficients a_n are unknowns to be determined.
In the following, we provide a high-level overview of the computational framework and the numerical implementation, focusing on the practical aspects relevant to our simulations. We deliberately omit technical details such as convergence proofs and error analysis. This choice is motivated both by the fact that such topics lie beyond the scope of this thesis, and by the

intrinsic difficulty of analyzing convergence in highly nonlinear systems, as those considered here.

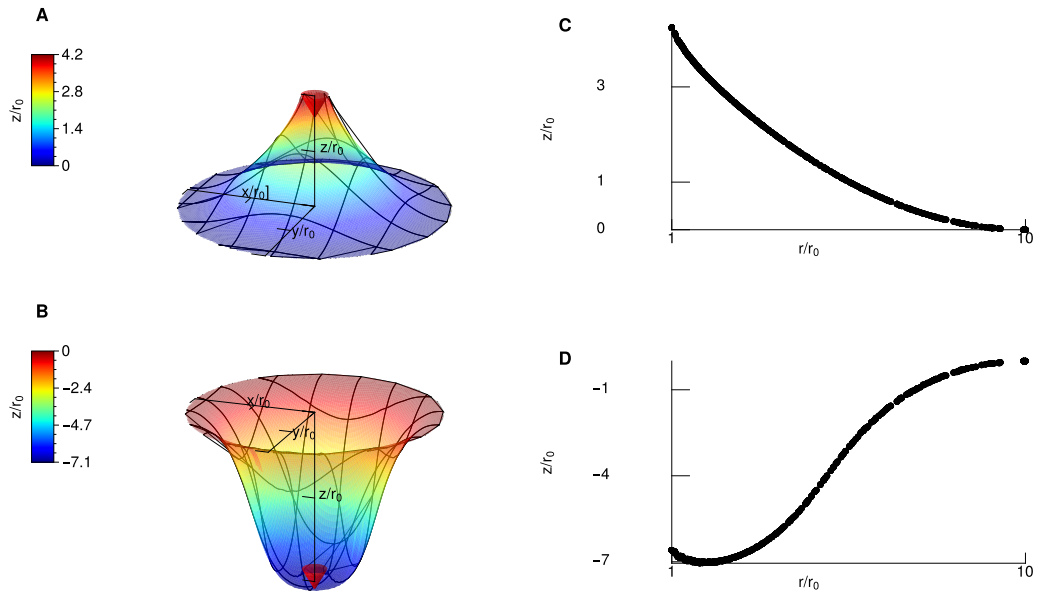

Figura 2.1: Example of membrane deformation induced by protein displacements. Case (A) corresponds to a displacement aligned with the imposed angle, enhancing membrane bending. Case (B) corresponds to a displacement opposite to the imposed angle.

2.1 General consideration about how it's implemented

2.1.1 Lagrange elements

The general procedure to derive the discrete equations from a system of PDEs follows the variational (or weak) formulation. The PDE is first multiplied by a test function (belonging to the same or a related function space as the trial function), and the resulting expression is integrated over the domain. Setting this integral to zero enforces the residual of the equation to be orthogonal to

the chosen function space.

Let $F_i(\psi) = 0$ the PDEs under study, the corresponding algebraic equations to be solved are:

$$\int_\omega F_i(\sum_n a_n \psi_n(\vec{r}))\phi_m(\vec{r})dS \tag{2.1}$$

And the unknown are the coefficients a_n. The finite-dimensional function space used for the discretization is the standard Galerkin space, which consists of continuous piecewise-polynomial functions defined on each element of the mesh. Specifically, we use Lagrange elements of order one. The choice of such elements allows to dealing easily with the resulting equations, indeed this element are piecewise polynomial of degree one and each of this is non-null just in a small number of mesh triangles.
As regard the mesh used, whenever the physical problem exhibits inherent geometric or physical symmetries (e.g., radial or reflection symmetries), the computational mesh is constructed to respect those symmetries.
This is essential to prevent the introduction of spurious asymmetries in the numerical solution that can arise purely from discretization artifacts. Moreover, it should be noted that unexpected asymmetries due to mesh anisotropy does not necessarily vanish with mesh refinement, expecially given the nonlinearity of the equations, which may amplify even minimal perturbations, causing instabilities in the convergence of the algorithm.

2.1.2 Well posedness of the variational problem and boundary conditions

Since there is no established theory for the well-posedness of the nonlinear problem under study, the number of boundary condition is going to be chosen considering an heuristic criterium, that is, starting from the linearized problem and assuming that the number of necessary boundary conditions does not change in the nonlinear case.
In our simulations, we impose two types of boundary conditions: Dirichlet and Neumann.
Dirichlet boundary conditions, which prescribe the value of the solution on the boundary, are typically enforced by restricting the function space to those functions that satisfy the conditions exactly. On the other hand, Neumann boundary conditions, which prescribe the value of normal derivatives or

fluxes, often emerge naturally as boundary terms when integration by parts is applied during the derivation of the weak form.
All the boundary conditions that did not arise naturally have been imposed using the Nitsche's method. This method adds a penalty term to the functional to enforce those conditions.

2.1.3 Dealing with higher-order equations

One common issue in finite element approximations is the limited regularity of the basis functions. For instance, standard elements (like Lagrange elements) are continuous in the function value but not in the first derivatives across element boundaries. This creates difficulties when the PDEs involves second or higher-order derivatives, and this is the case with the equation under study, since the equation for the curvature is fourth-order.

To address this, when possible, integration by parts is applied to reduce the order of derivatives required on the trial, shifting derivatives onto test functions and introducing boundary or interface terms.
However, in the case under study, integration by parts is not enough, for this reason, auxiliary fields have been introduced.
These fields are coupled to the primary solution through additional equations or constraints that ensure that they approximate the desired derivatives in a weak sense.

2.2 Implementation in FEniCS

The tool used to implement the finite element method is FEniCS, an open-source Python's library that allows for high level definition of the variational problem and automatic solution of the resulting system of equations.
The fully nonlinear equation presented in the previous section have been implemented.
The library [4] used to solve the equations had already been developed and validated by the internship supervisor, the contribution of the student has been to extend parts of the code and adjust some existing ones.

2.2.1 Limitations of the numerical scheme used

Two main limitations have been encountered due to the chosen scheme:
Due to the high non-linearity of the equations the algorithm did not converge for certain boundary conditions and for mesh dimensions relatively thin. For this reason, an increasing number of evaluations have been performed to reach a sufficiently small error and convergence.
The use of the Monge parametrization for the description of the membrane caused issues with overhangs (points where $\partial_r z$ assumes high values). This is reflected in some limitations in the boundary conditions imposed (for example, the displacement of the protein could not be much larger than the dimension of the external boundaries).
This problem could have been solved using a general parametrization of the form:

$$\sigma = (x(u, v), y(u, v), z(u, v)) \tag{2.2}$$

However, this would have required a radical change of the code.

Capitolo 3

Steady state solution no flow

In static condition, that is, where no flow of phospholipids is present, the equation reduces to the balance of surface stresses and bulk forces, that is:

$$\nabla^i \nabla_i H + 2H(H^2 - K) - H\frac{\sigma}{\kappa} = 0 \tag{3.1}$$

It is well known that one can distinguish between regimes where the bending energy totally dominates and regimes where the elastic tension play a role too. The threshold is setted by the length $\ell = \sqrt{\frac{\kappa}{\sigma}}$.
Give the values of κ and σ from table 1.1, this length is of the order of $10r_0$[1].

3.1 Radial symmetry

One can study equation 3.1 in the case where the membrane inclusion has a circular cross section. In this situation, the system is expected to exhibit radial symmetry, for this reason, it is convenient to use the Monge parametrization in polar coordinates, namely:

$$\vec{x}(r, \theta) = (r\cos(\theta), r\sin(\theta), z(r, \theta)) \tag{3.2}$$

[1] r_0 is the typical radius of a trans-membrane protein

In particular, we expect $z(r,\theta) = z(r)$. Under this assumption, the equation assumes the following form:

$$\frac{1}{\sqrt{|g|}}\partial_r(\sqrt{|g|}g^{rr}\partial_r H) - 2H(H^2 - K) + H\frac{1}{\ell^2} = 0 \tag{3.3}$$

Where the geometrical quantities are:

$$\begin{cases} \omega = \partial_r z \\ \sqrt{g} = r\sqrt{\omega^2+1} \\ g^{rr} = \frac{1}{1+\omega^2} \\ H = \frac{1}{2}\left[\frac{\partial_r\omega}{(1+\omega^2)^{3/2}} + \frac{\omega/r}{(1+\omega^2)^{1/2}}\right] \\ K = \frac{\omega\partial_r\omega}{r(1+\omega^2)^2} \end{cases}$$

Equation 3.3 cannot be easily solved, however, it can be simplified by considering small values of ω. This assumption is valid both when the displacement of the protein relative to the reference plane and the imposed angle are small, and when one aims to study the behavior of the membrane far from the protein, where the membrane is expected to be nearly flat. If the slope is small the geometrical quantities become:

$$\begin{cases} \omega = \partial_r z \\ \sqrt{g} \sim r + o(\omega) \\ H = \frac{1}{2}\left[\partial_r\omega + \frac{\omega}{r} + o(\omega)\right] \\ K = o(\omega) \end{cases}$$

Substituting into the equation 3.3, one obtains the following third-order linear differential equation:

$$\left(1 - \frac{r^2}{\ell^2}\right)\omega - r\left(1 + \frac{r^2}{\ell^2}\right)\omega' + 2r^2\omega'' + r^3\omega''' = 0 \tag{3.4}$$

The equation for $z(r)$ is a fourth-order equation, that is, four boundary conditions should be imposed to have a unique solution. Physically relevant BCs are the following:

$$\begin{cases} z(r_0) = h_0 \\ z(R) = 0 \\ \omega(r_0) = \tan\alpha \\ \omega(R) = 0 \end{cases}$$

- $z(r_0) = h_0$, this condition is physically relevant because one could be interested in situation when the protein is constrained at a certain position due to the presence of an external force [2];

- $z(R) = 0$, solutions of the equation (3.4) are invariant under translation along the z axis, this BC simply fix the reference z plane.

- $\omega(r_0) = \tan(\alpha)$, some transmembrane proteins that are much more rigid than the membrane have shapes that force certain angles when bounded to the membrane [7].

- $\omega(R) = 0$, this condition intrinsically fixes the length scale of the external environment, indeed, the presence of a distance at which the slope of the membrane is zero implies that there are external torques applied to the membrane[3].

The equation admits three linear independent solutions, one of which is $\omega = \frac{1}{r}$.
The remaining two independent solutions can be found reducing the order of the equation through the substitution $\omega = \frac{\omega^*(r)}{r}$.
The resulting equation is:

$$\frac{\left(1 - \frac{r^2}{\ell^2}\right) S(r) + r\left(-S'(r) + r\, S''(r)\right)}{r^3} = 0 \tag{3.5}$$

Where $S(r) = \frac{d\omega^*}{dr}$.
Solutions to this equation can be found in Taylor series form, calculations lead to the following expressions[8]:

$$S_1(r) = \sum_{k=0}^{+\infty} \frac{\ell^{-2k}}{(2k!!)^2} r^{2k+1} \tag{3.6}$$

$$S_2(r) = S_1(r) \int \frac{x}{S_1(x)^2} dx \tag{3.7}$$

[2]One could also consider fixed forces, that is almost the same intuitively but mathematically less trivial to impose

[3]External torque can be due to the presence of other proteins or the actin cortex that increases the rigidity of the membrane.

Written in this form they are not particular informative, however, analysis of the asymptotic behavior4.3.1 gives the following results:

$$S_1(r) \sim e^{\frac{r}{\ell}}\sqrt{r} \quad \text{for } r \to +\infty \tag{3.8}$$
$$S_1(r) \sim r \quad \text{for } r \to +\infty \tag{3.9}$$
$$S_2(r) \sim e^{-\frac{r}{\ell}}\sqrt{r} \quad \text{for } r \to 0 \ (\ell \to +\infty) \tag{3.10}$$
$$S_2(r) \sim r\ln(r) \quad \text{for } r \to 0 \ (\ell \to +\infty) \tag{3.11}$$

It is interesting to note that only the membrane shape corresponding to the solution $S_2(r)$ tends to zero at $+\infty$. Hence, one can expect the membrane to decay exponentially far from the protein ($r \gg \ell$).
Given the linearity of the equation, the solution satisfying conditions 3.1 can be written as a linear combination of the linear independent functions, weighted by the coefficients:

$$c_i = B_i(R, r_0)h_0 + C_i(R, r_0)\tan\alpha \tag{3.12}$$

One can note that final solution will be linear in h_0, $\tan\alpha$, while it will have some nonlinear dependence on R and r_0.

3.2 Non-linear behavior

3.2.1 Approximate solution for large gradients

Further insight about the non-linear behavior of the membrane can be obtained through the substitution $\omega = \frac{\psi}{\sqrt{1-\psi^2}}$. Under this substitution the various geometrical quantities assume the form:

$$\begin{cases} \omega = \partial_r z \\ \sqrt{g} = \frac{r}{\sqrt{\psi^2+1}} \\ g^{rr} = 1 + \psi^2 \\ H = \frac{1}{2}\left[\partial_r\psi + \frac{\psi}{r}\right] \\ K = \frac{\partial_r\psi^2}{2r} \end{cases}$$

Substituting into the equation one finds:

$$(1-\psi^2)\partial_r^2 H + \left(\frac{1-\psi^2}{r} - \psi\partial_r\psi\right)\partial_r H + \\ + \left(\frac{2\psi\partial_r\psi}{r} + \frac{1}{\ell} - 2H^2\right)H = 0 \tag{3.13}$$

$$H = \partial_r\psi + \frac{\psi}{r} \tag{3.14}$$

The latter equation admits a zero curvature solution of the form $\psi = \frac{c_1}{r}$. This solution can be used to gain insight into the exact non-linear solution. The profile of the membrane is given by:

$$z(r) = -c_1 \ln\left(\frac{r - \sqrt{r^2 - c_1^2}}{c_2}\right) \tag{3.15}$$

The two coefficients c_1 and c_2 can be determined by imposing the boundary conditions:

$$\begin{cases} z(R) = 0 \\ \omega(r_0) = \tan\alpha \end{cases} \tag{3.16}$$

It turns out to be advantageous to linearize this new equation. In the previous case, the linearization was justified for small values of $\omega \ll 1$, where nonlinear terms were negligible. However, in the present case, the transformation maps the unbounded interval $(-\infty, +\infty)$ to the finite interval $(-1, 1)$, effectively compressing the domain. As a result, the omitted nonlinear terms (of order $O(\psi^3)$) remain relatively small even for higher values of ω. Therefore, we may expect the linearized solution to remain valid over a broader range of ω. The linearized equation is the same as that obtained in the previous section. The final solution will be of the form:

$$\omega = \frac{c_1 f_1(r) + c_2 f_2(r) + c_3 f_3(r)}{\sqrt{1 - (c_1 f_1(r) + c_2 f_2(r) + c_3 f_3(r))^2}} \tag{3.17}$$

Where $f_i(r)$ are the solution already described in section 3.1.
One can note that this solution develops singularities wherever $\psi(r) = 1$. In the next section, this solution is compared with the numerical one.

3.3 Numerical results

To assess the regime of validity of the theoretical results, several numerical simulations were performed and the resulting membrane profiles were compared with the analytical predictions (figure 3.1).
In figure 3.1, it can be seen that the linear solution remains accurate for imposed inclination angles of up to approximately $\tan\alpha \simeq 0.4$.
Beyond this threshold, the linear approximation fails to capture the actual shape of the membrane, as non-linear effects become significant. In contrast, the non-linear solution given in equation 3.17 closely reproduces the membrane profile even for larger imposed angles. This form could be particularly relevant for describing a regime where large deformation are present.

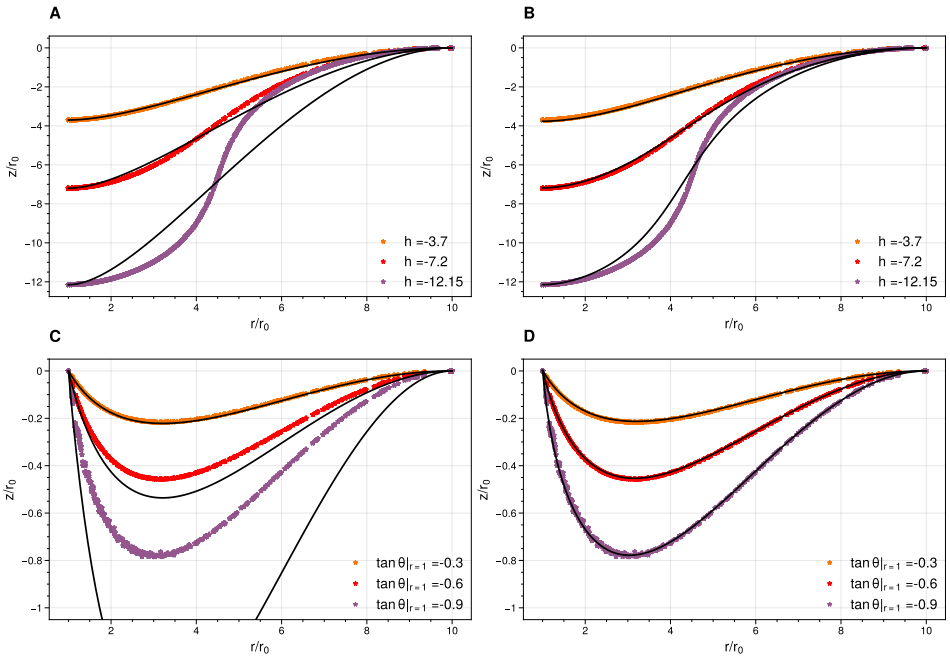

Figura 3.1: Comparison between analytical and numerical membrane shapes for different values of the imposed inclination angle (C, D) and imposed displacement (A, B). In (A, C) the numerical result is compared with the solutions to the linearized equation, while in cases (B, D) they are compared with the nonlinear approximate solutions.

3.4 Expansion near a vertical flex

It is interesting to study the solution near a point where $\frac{\partial z}{\partial r} \to \infty$ since, as will also be noted in the next section, the membrane tends to form tubules for a large enough displacement of the protein.
In order to do this, it is convenient to perform a change of variable, considering z the independent variable and $r = r(z)$. After this substitution and linearization ($r(z) = r_* + u(z)$, where $u << R$) the equation becomes:

$$\frac{2 - \frac{r_*^2}{\ell^2}}{r_*^3} - \left(\frac{6 - \frac{r_*^2}{\ell^2}}{r_*^4}\right) u - \left(\frac{5 - \frac{r_*^2}{\ell^2}}{r_*^2}\right) u''(z) - u''''(z) = 0 \tag{3.18}$$

Since $u << R$, in order for the equation to be satisfied, the term of order $O(1)$ must vanish, that is $r_0 = \sqrt{2}\ell$. This result fixes the dimension of an energetically stable tubule, indeed, if $r_0 \neq \sqrt{2}\ell$, necessarily at least one term between u'' and u'''' should be of order $O(1)$ to balance the constant term. This would not be consistent with the fact the terms proportional of order $O(u''^2)$ has been neglected.
Solutions of the equation are discussed in more detail in the appendix 4.3.1.

3.5 Forces

One of the physical quantities that describes the interaction between the protein and the membrane is the force at the boundary. The latter have been derived in the appendix 4.3.1 using a variational approach. The tangential and normal components of the force per unit length are:

$$\begin{cases} \vec{f_\perp} = 2\kappa n^i \nabla_i H \hat{n} = -2\kappa \partial_r H \hat{n} \\ \vec{f_\parallel} = -n^i (2\kappa H^2 + \sigma) \vec{e_i} \end{cases}$$

Using dimensional analysis one finds that the dependence of the force density on the height should have the form:

$$f(h_0, \sigma, \kappa, R, r, \tan\alpha) = \frac{\kappa}{R^2} \phi \left(\frac{\sigma}{\kappa} R^2, \frac{h_0}{R}, \frac{r}{R}, \tan\alpha\right) \tag{3.19}$$

Integration over the circular boundary leads to:

$$\begin{cases} F_\perp^z = 2\pi\kappa \frac{r_0}{R^2} \phi_\perp \left(\left(\frac{R}{\ell}\right)^2, \frac{h_0}{R}, \tan\alpha\right) \cos\alpha \\ F_\parallel^z = 2\pi\kappa \frac{r_0}{R^2} \phi_\parallel \left(\left(\frac{R}{\ell}\right)^2, \frac{h_0}{R}, \tan\alpha\right) \sin\alpha \end{cases} \tag{3.20}$$

From this form of the force one can note that, given the independent variables, different regimes have to be expected:

- $R \lesssim \ell$: this regime could describe situations where proteins are packed or σ is very small.
- $R \gg \ell$: this regime corresponds to situations where the membrane inclusion is almost isolated.

At the same time, for a given value of the ratio $\frac{R}{\ell}$ one can have different force regimes depending on the ratio $\frac{h_0}{R}$.
In the next section the precise behavior of the force is evaluated numerically and this different regimes are found.

3.5.1 Numerical results

In the non-linear regime, the force exerted by the membrane has been evaluated numerically. The results are shown in Figure 3.2.

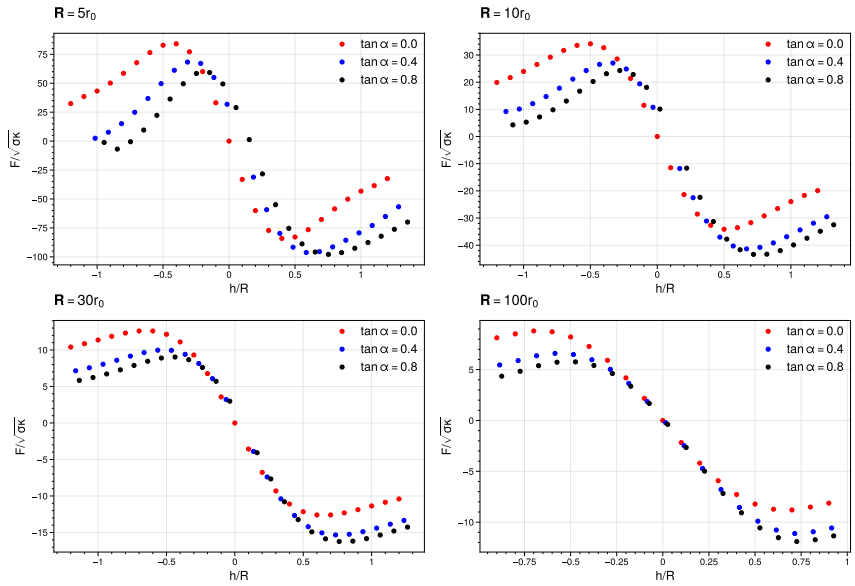

Figura 3.2: Numerical evaluation of the total force along the z-axis for different values of ω, h and R.

The total force along the z-axis (the only nonzero component due to rotational symmetry) exhibits a non-monotonic dependence on the displacement

h of the protein. As expected, the force is asymmetric under the inversion $h \to -h$ when the angle α is nonzero.

For small displacements, the force scales linearly with h, and the slope decreases with increasing R. In contrast, for large displacements, the force develops oscillations whose amplitude decreases with R. This oscillatory behavior at large h is consistent with previously reported results in the literature. For instance, in [1], where a point-like force is applied to a membrane, similar oscillations and a relaxation to a constant force for $h \to +\infty$ are observed.

Due to limitations in the current version of the library, as discussed in section 2.2.1, it was not possible to explore the asymptotic regime for very large values of h.

3.6 Tubule formation

From the numerical analysis of the pulling force, one can observe the existence of a threshold height h_{thr} above which the force ceases to increase and instead starts to decrease.
This transition is accompanied by a qualitative change in the shape of the membrane. In particular, the system shifts from a regime characterized by distributed curvature gradients to one dominated by localized, sharp curvature variations, as shown in figure 3.3. This regime marks the onset of tubule formation, a well-known phenomenon in membrane mechanics.

To gain insight into this transition, we consider a simplified model that captures the competition between distributed and localized gradients. Inspired by the numerical profiles, we divide the radial interval $[r_0, R]$ into three distinct regions:

- $[r_0, l - \frac{h}{|x|}]$: although the curvature here is not exactly zero, due to the energetic cost of satisfying the boundary conditions, this region remains relatively short and nearly flat. For simplicity, we approximate it as flat.

- $[l - \frac{h}{|x|}, l]$: this is the transition region, where the membrane exhibits curvature. We assume the membrane has a constant slope x in this region.

- $[l, R]$: here, the curvature is again negligible, and the membrane is nearly flat.

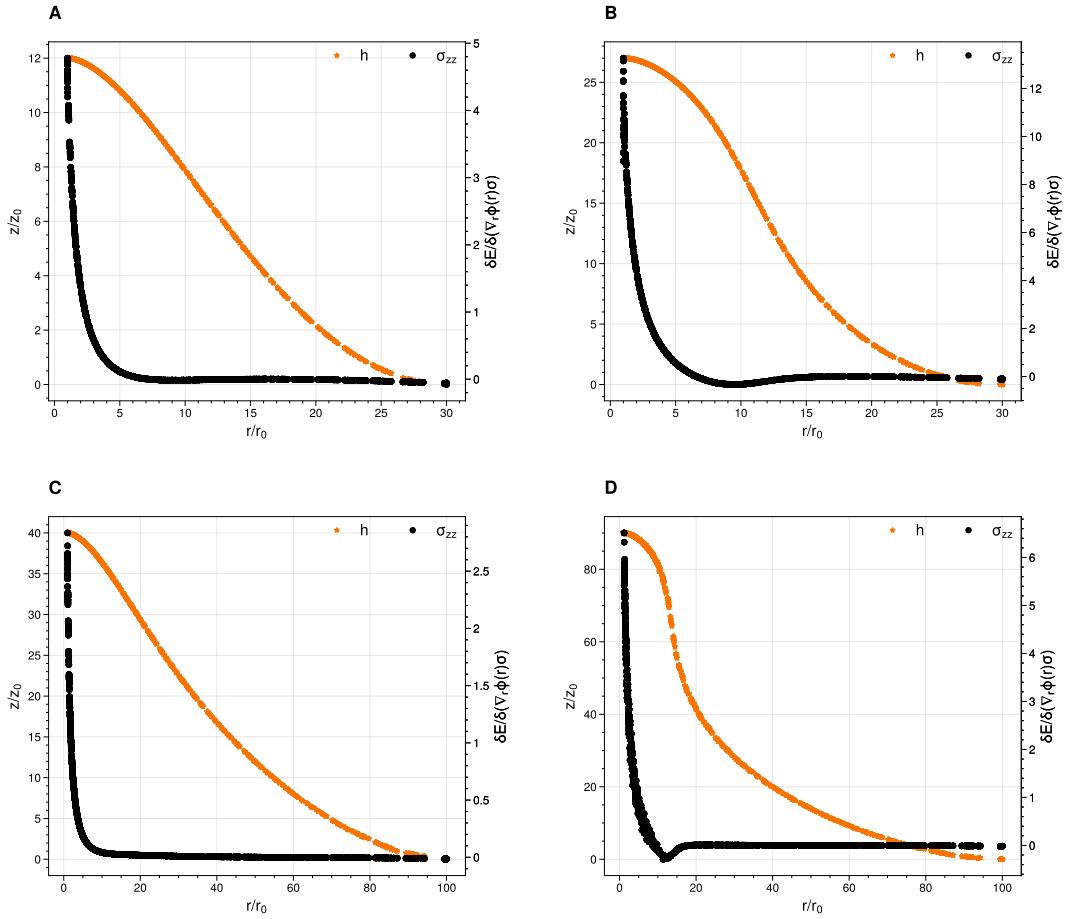

Figura 3.3: Membrane shape and normal stresses evaluated for different values of the protein displacement and mesh dimension. Figures (A) and (B) correspond to $R = 30r_0$, figures (C) and (D) to $R = 100r_0$.

In this model, x denotes the average slope in the transition region, and l its extent. The total energy of the system includes two contributions:

$$E_H = 2\pi\frac{k}{2}\int_1^R \sqrt{g}\, H^2\, dr \quad \text{(bending energy)} \tag{3.21}$$

$$E_\sigma = 2\pi\sigma\int_1^R \sqrt{g}\, dr \quad \text{(tension energy)} \tag{3.22}$$

where H is the mean curvature and $\sqrt{g}$ the metric factor.

Using the above approximations, the energy can be reduced to a closed

expression:

$$E(x, l, h) = \ell^{-2} \left(\frac{h^2}{x^2} - \frac{2hl}{x} \right) (1 - \sqrt{1 + x^2}) - \frac{x^2 \ln\left(1 - \frac{h}{lx}\right)}{\sqrt{1 + x^2}} \tag{3.23}$$

The equilibrium configuration corresponds to the values (x^*, l^*) that minimize this energy. By solving this minimization problem numerically for various values of h and ℓ, one finds that for large ℓ (i.e., large domain), there exists a threshold height h_{thr} above which localized gradients (tubule) become energetically favorable.

However, as ℓ increases, the energetic cost associated with the increased surface area due to these sharp gradients becomes comparable to that of distributed curvature, penalizing the formation of very steep localized regions. As a consequence, the threshold height h_{thr} increases with ℓ.

In addition to predicting the onset of tether formation, this simplified model also captures the qualitative behavior of the force-height relationship observed numerically. In particular, consider the two limiting cases:

- For $h < h_{\text{thr}}$, with $h \ll \ell$, we expect a small slope $x \sim \frac{h}{R}$. Expanding the curvature, we find:

  $$H \simeq H_0 + A(\ell)\frac{h^2}{R^2} + \mathcal{O}\left(\frac{h^4}{R^4}\right)$$

  leading to a linear force–height relation.

- For $h > h_{\text{thr}}$, the system minimizes its energy by forming a narrow neck, and we expect $x \to \infty$. In this limit:

  $$H \simeq B(c^2, \ell) \cdot h + \mathcal{O}(1/x)$$

  and the force becomes approximately constant with height.

This matches well with the numerical force curves (figure 3.2), especially for large values of R.

3.7 Membrane-mediated interaction between two proteins

When two proteins are present, the assumption of rotational symmetry no longer holds. As a result, the partial differential equation cannot be reduced

to an ordinary differential equation, and the analytical treatment of the problem becomes considerably more complex. Therefore, this case will be investigated numerically in the following.
The presence of two proteins is expected to give rise to a membrane-mediated interaction between them. For $R \ll \ell$, the deformation induced by a single protein decays exponentially, and so does the interaction [9].
However, since situation where the distance between the two proteins is of the order or smaller then ℓ could occur (regimes where the density of membrane inclusion is high), it is of interest to study how the potential energy depends on their separation.
To this end, we numerically compute the energy of the system, by evaluating the integral:

$$U(d) = \int_\Omega \left(\frac{\kappa}{2}H_2^2 + \sigma\right)\sqrt{g}dS - 2\int_\Omega \left(\frac{\kappa}{2}H_1^2 + \sigma\right)\sqrt{g}dS \tag{3.24}$$

Where H_2 is the curvature distribution in the presence of two proteins separated by a distance equal to d, while H_1 is the curvature in the case of a single protein, It has been subtracted in such a way to have potential that is null at infinity.
Two situations were analyzed, when the proteins impose angles with same or different orientations (figure 3.4).

The numerical evaluation gives the potential shown in figure 3.5. One can note that there seems to be a divergence for. As can be noted, the angle imposed by each of the protein seems to be equivalent to a sort of "charge" possessed by the protein, in the sense that proteins that impose angles with the same orientation tend to repel while proteins that impose opposite angles tend to attract.
The dependence of the interaction strength on the tangent of the angle can be seen in figure 3.5).

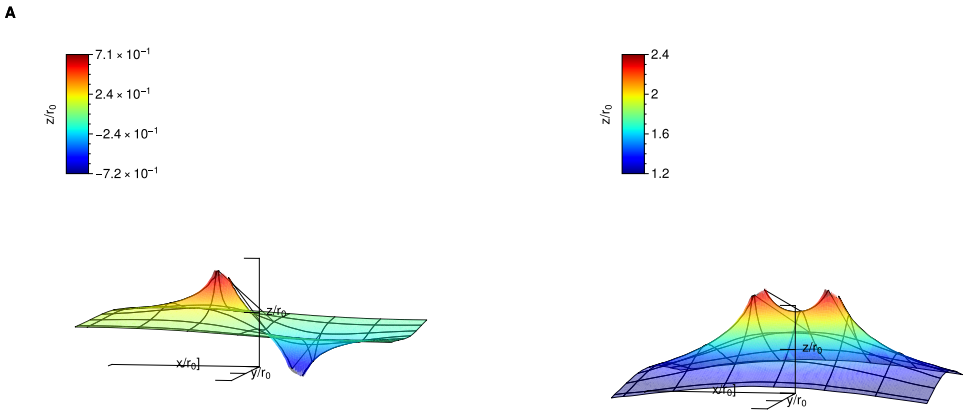

Figura 3.4: Membrane profile for different proteins orientations. In (A) the proteins impose angles with different orientations, while in (B) the same orientation.

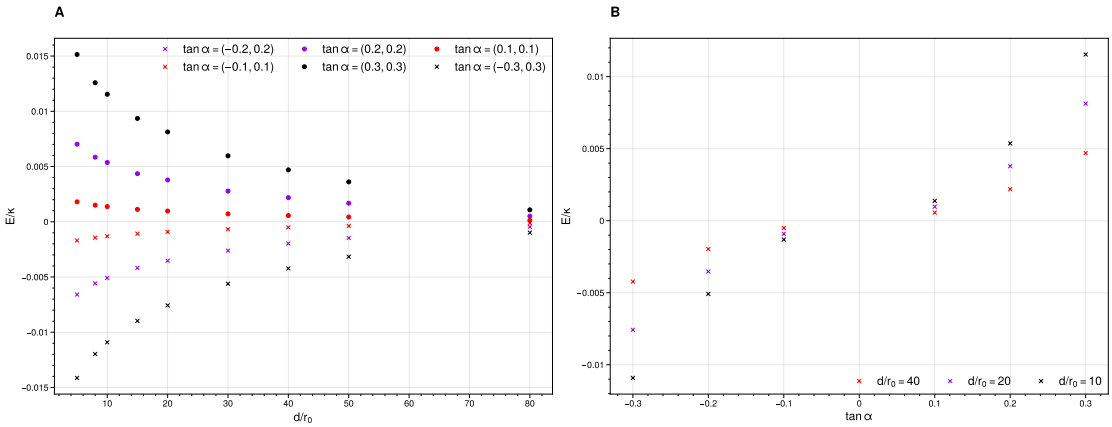

Figura 3.5: Figure (A) represents the membrane energy as a function of the proteins separation for different values of the angles. Figure (B) shows the membrane energy as a function of the angle of one of the two protein when the other is kept fixed.

Capitolo 4

Steady state solution with flow

4.1 Equation and boundary conditions

In the case of a stationary tangential flow the equations become:

$$\begin{cases} \nabla_i v^i = 0 \\ \mathrm{Re} v^j \nabla_j v^i = \nabla^i \mathrm{Re}\sigma + \left(\nabla^j \nabla_j v^i + 2K v^i\right) \\ w = 0 \\ \mathrm{Re} v^i b_{ik} v^k = -\mathrm{A}\left(2\nabla^i \nabla_i H + 4H(H^2 - K)\right) \\ \qquad\qquad + 2H\mathrm{Re}\sigma + 2\, b_{ij}\nabla^i v^j \end{cases}$$

A system with a square internal boundary will be considered in the following analysis (figure 4.1). The reference frame is taken to be that of the protein, meaning that the flow around the protein is studied as if the protein were stationary and the surrounding fluid is moving. The following boundary conditions will be imposed:

- $\vec{v} = 0$ at the boundary of the protein. This no-slip condition reflects the assumption that phospholipids in direct contact with the protein are immobilized due to binding interactions.
- $\vec{v} = v_0 \hat{x}$ at $x = -L/2$. Far upstream from the protein, the velocity field is assumed to be uniform and unperturbed, modeling the background flow of the membrane in the absence of the obstacle.

- $\sigma = \sigma_0$ at $x = R/2$. Far downstream, the stress is prescribed to match the unperturbed flow conditions, under the assumption that the influence of the obstacle vanishes sufficiently far away.
- $\vec{v} \cdot \hat{y} = 0$ at $y = \pm R/2$. This condition enforces confinement in the transverse (y) direction, modeling either the finite extent of the membrane patch or the presence of physical barriers. It introduces a geometric/environmental length scale, R.
- Fixed contact angle at both the protein boundary and the external boundary. This boundary condition reflects mechanical equilibrium of the interface with the protein and the environment, and it controls the slope of the membrane surface at the contact line.
- Fixed height at the external boundary. This boundary condition sets the reference level for the membrane profile.

4.2 Linearized equation

Like in the case of two proteins, also if a flow along the x direction is present, the hypothesis of radial symmetry is not valid anymore. In this case, the velocity field and the various geometrical quantities will depend both on the angle and the distance from the center of the protein.
To gain insight, it is convenient to consider small deviations from the plain configuration, that is, to linearize the various quantities around $\omega = 0$ in the Monge representation.
To first order in the Monge representation, the equations reduce to:

$$\begin{cases} \partial_i v^i = 0 \\ \mathrm{Re}\, v^j \partial_j v^i = \partial_i \sigma \mathrm{Re} + \nabla^2 v^i \\ \mathrm{Re}\, v^i b_{ik} v^k = -2\mathrm{A}\nabla^2 H + \\ \qquad\qquad + 2H(\sigma \mathrm{Re}) + 2\, b_{ij} \partial_i v^j \end{cases} \tag{4.1}$$

From the second equation, one can see that the velocity field does not feel the curvature of the membrane to first order. The two equation will be really coupled only when $K * v^i$ is comparable to unity.

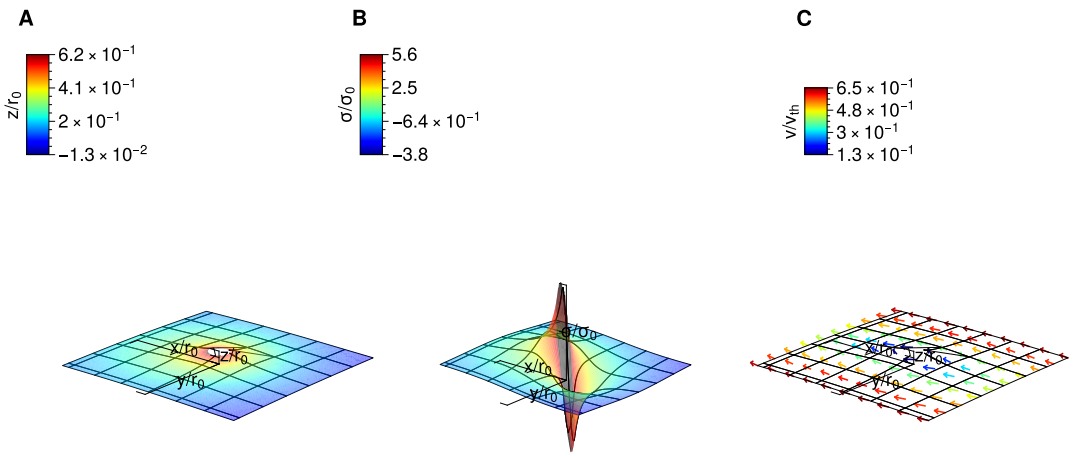

Figura 4.1: Figure (A) represents the membrane shape in the presence of the flux. Figure (B) shows the value of the membrane tension, in the presence of the flux is not constant anymore. Figure (C) shows the three dimensional flow distribution. All the figures correspond to flux velocity equal to v_{th}

Given the fact that $\mathrm{Re} \ll 1$ one can neglect the term on the left side of the second equation and reduce the number of equations using a well known mathematical trick [10].
First of all, it is convenient to introduce the current function:

$$v_x = \partial_y \psi \tag{4.2}$$

$$v_y = -\partial_x \psi \tag{4.3}$$

By introducing this function, the continuity equation is trivially satisfied. Moreover, taking the curl of the second equation gives the final equation:

$$\nabla^2 \nabla^2 \psi = 0 \tag{4.4}$$

The equation for σ can be obtained by taking the divergence of the second equation of 4.1.

The final form of the equations is:

$$\begin{cases} \nabla^2\nabla^2\psi = 0 \\ \nabla^2\sigma' = 0 \\ \mathrm{A}\nabla^2 H = H\sigma' + 2\epsilon^{kj}(\partial_i\partial_j z)(\partial_i\partial_k\psi) \end{cases}$$

where we neglected $\mathrm{Re}\, v^i b_{ik} v^k$ given the value of Re. Even though the equations have been significantly simplified, an analytical study will not be pursued. Instead, a numerical analysis will be carried out.

4.3 Numerical results

Numerical simulations were made for different values of v and R (figure 4.1), showing that three different regime are present for the membrane shape (figure 4.2):

- $v \ll v_{th}$: The flow has no visible effect on the membrane shape.
- $v \simeq v_{th}$: The membrane shape begins to show asymmetry due to the presence of the flow.
- $v > v_{th}$: The membrane is strongly affected by the flow, leading to the formation of a bump.

Figure 4.2 shows the membrane shape for different values of v. The flow field has also been evaluated and compared for different velocities (Figure 4.3). As expected from equations 4.1, even after the formation of the bump, the flow field is qualitative the same.
The previous result can be explained considering the energetic competition between tension and bending energies. Indeed, due to the presence of the flow, a region of negative tension appears where the flow encounters the protein (figure 4.1).
Negative tension implies that the membrane tends to invaginate, leading to an increase in local density and thus a local bending of the membrane. Comparing the orders of magnitude of the surface tension σ and the bending rigidity suggests that this deformation is energetically favorable under certain conditions. This reasoning allows one to define a characteristic length scale from the physical parameters:

$$l = \frac{k}{\eta v} \tag{4.5}$$

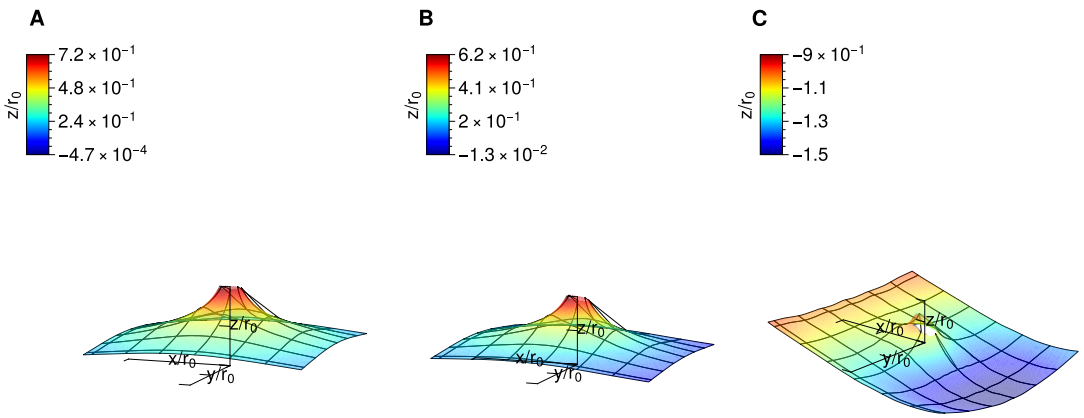

Figura 4.2: Membrane shape for different values of the flux velocity. Figure (A) is for velocity equal to $0.1v_{th}$, (B) for v_{th} and (C) for $5v_{th}$

By comparing this length scale l with the other relevant length scale R, one can determine the velocity regimes in which membrane deformation is expected to occur, that is, when $l < R$.

4.3.1 Forces

The total viscous force applied to the protein has been numerically evaluated and is shown in figure 4.4.
One can note that the force increases linearly with the velocity up to values of $10v_{th}$ and changes in the angle imposed by the membrane inclusion does not significantly affect the total force. This is again in accordance with the fact that this is a regime in which the equations can be linearized and the flow is not dependent on the membrane shape. The slope of the force as a function of the velocity is also shown in Figure 4.4, and is in agreement with the result reported in [11].
They analytically studied a system with a similar setting: the flow of a cylinder of radius r_0 in a channel of width R with smooth walls, finding that

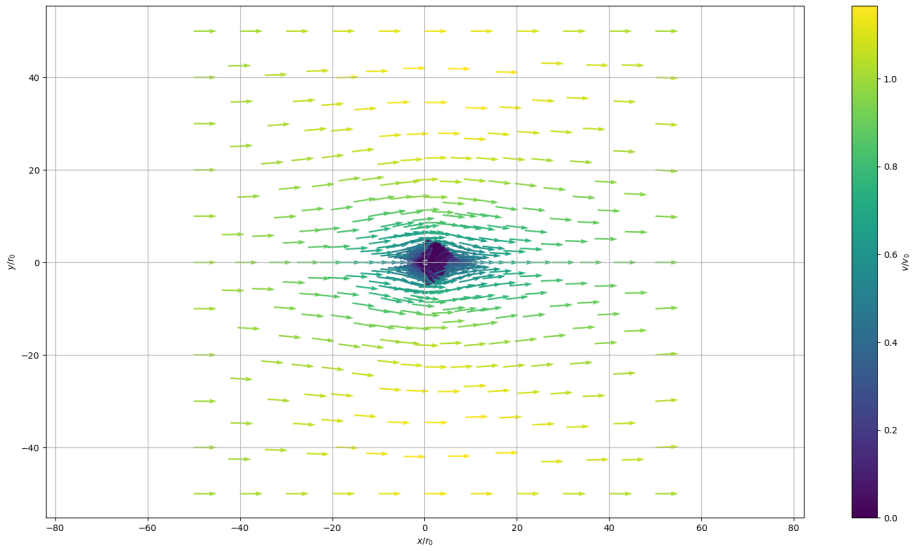

Figura 4.3: Flow field projected into the xy plane.

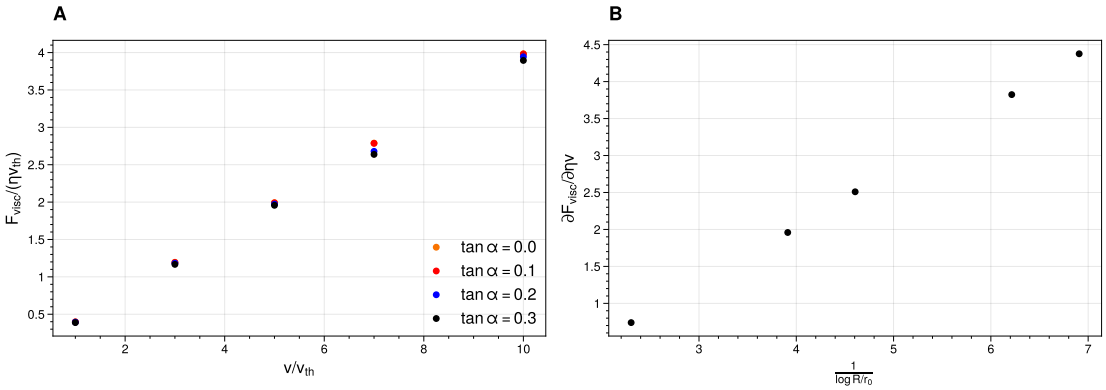

Figura 4.4: Figure (A) shows the dependence of the viscous forces on the flux velocity for different values of the angle imposed by the protein. Figure (B) shows how the slope of the force varies with the dimension of the external boundary of the mesh.

the viscous force on the cylinder scales as $\frac{1}{\log \frac{R}{r_0}}$.

Conclusion

This thesis has addressed two key aspects of protein-membrane mechanics: static deformation induced by protein inclusions and the effect of membrane flow on protein mobility.

In the static regime, we confirmed that the inclusion of finite size and anchoring angles significantly alters the resulting membrane profile and forces in cases when deformations are of the order of magnitude of the inclusion or the membrane is constrained at distances smaller than ℓ. Analytical approximations proved effective for small deformations, while numerical simulations were essential for exploring the nonlinear regime.
The results show that the forces experienced by proteins are sensitive not only to the membrane geometry but also to the boundary conditions imposed at its edge. This indicates that protein concentration and spacing may regulate not only inter-protein interactions but also how the cell mechanically engages with its environment. For instance, a decrease in the spacing between proteins leads to an increase in the slope of the force-displacement curve in the linear regime, corresponding to a stiffer attachment to the membrane. Such a mechanism could enable cells in tissues to dynamically regulate tissue-level elasticity.

We also observed the well known transition to tubule formation beyond a critical displacement, characterized by a sharp change in curvature and stress distribution. This behavior was captured both numerically and through a minimal model.

Finally, we quantified the interaction between membrane inclusions in a regime where analytical treatment is challenging. We confirmed the expected exponential screening for distances $d > \ell$ and studied the curvature-mediated interaction at small separations between the inclusions. Unfortunately, it was not possible to verify the fluctuation induced interaction scaling as $U(r) \sim \frac{1}{r^4}$ found in [9], since our approach does not account for fluctuations.

In the dynamic regime, we found that membrane flow induces additional

shape deformations when the velocity exceeds a threshold. Importantly, the viscous force exerted on the protein follows a linear trend with respect to the flow speed, and its scaling with system size matches analytical predictions for confined geometries.

Even though extreme regimes ($h \gg R$, $v \gg v_{th}$) could not be explored due to limitations of the approach used, modifications to the library could enable the study of these regimes. Moreover, the library supports the analysis of situations involving more than two proteins. Indeed, it allows easy generalization to complex domains containing large numbers of proteins.

Appendix

Summary of useful differential geometry facts

This section summarizes key results from differential geometry that are employed throughout this work. We consider a general two-dimensional manifold embedded in three-dimensional Euclidean space, $\mathbb{R}^3$, which can be parametrized by a smooth map $\Sigma : \mathbb{R}^2 \to \mathbb{R}^3$. A point on the surface is described by a position vector $\vec{r}(x^1, x^2)$, and a natural basis for the tangent space at each point is provided by the partial derivatives with respect to the coordinates:

$$\vec{e}_i = \frac{\partial \vec{r}(x^1, x^2)}{\partial x^i}, \tag{6}$$

$$\hat{n} = \frac{\vec{e}_1 \times \vec{e}_2}{|\vec{e}_1 \times \vec{e}_2|}, \tag{7}$$

where $\hat{n}$ denotes the unit normal vector to the surface. It is important to note that these basis vectors carry physical dimensions. Any three-dimensional vector field $\vec{V}$ defined on the surface can be decomposed into components parallel and perpendicular to the surface:

$$V^i_{\parallel} = \vec{V} \cdot \vec{e}^{\,i} = V^\alpha e^i_\alpha, \tag{8}$$

$$V_\perp = \vec{V} \cdot \hat{n} = V^\alpha n_\alpha. \tag{9}$$

To avoid confusion between components in three-dimensional space and those in the tangent space, latin indices will be used for the latter, while Greek indices will denote components in $\mathbb{R}^3$.

We now consider the behavior of geometric quantities under an infinitesimal deformation of the surface, expressed as

$$\delta\vec{r} = \phi^i \vec{e}_i + \psi\hat{n},$$

where ϕ^i and ψ are small perturbation fields defined on the surface.

From the surface parametrization, two fundamental second-order tensor fields can be introduced:

- The *first fundamental form*, which defines the surface metric:

$$g_{ij} = \vec{e}_i \cdot \vec{e}_j,$$

- The *second fundamental form*, which encodes the curvature:

$$b_{ij} = \partial_i \hat{n} \cdot \vec{e}_j.$$

Special care must be taken when computing derivatives of vector or tensor fields. Since the basis $\{\vec{e}_i\}$ changes from point to point, partial derivatives of the vector components alone do not capture the total variation of a field. To address this, one introduces the *Christoffel symbols*, defined by

$$\Gamma^k_{ij} = \vec{e}^{\,k} \cdot \partial_i \vec{e}_j,$$

which account for the spatial variation of the basis vectors themselves. Using the Christoffel symbols, the *covariant derivative* of a vector field v^j on the surface is given by

$$\nabla_i v^j = \vec{e}^{\,j} \cdot \partial_i (v^k \vec{e}_k),$$

which properly describes how the vector field changes when both the field and the basis vary across the surface. Starting from the second fundamental form, one can define two geometrical quantities that are used to characterize the extrinsic geometry of the surface, these are:

- The *mean curvature* H, defined as the trace of the second fundamental form:

$$H = \frac{1}{2} g^{ij} b_{ij},$$

  where g^{ij} is the inverse of the first fundamental form.

- The *Gaussian curvature* K, defined as the determinant of the second fundamental form:

$$K = \det(b_{ik} g^{kj}).$$

Finally, we consider the first-order variations of key geometric quantities under the perturbation $\delta\vec{r} = \phi^i\vec{e}_i + \psi\hat{n}$ which are used to evaluate the variation of the Helfrich-Canham energy functional.
These include:

$$\delta\vec{e}_i = (\nabla_i\phi^k - \psi b_i^k)\vec{e}_k + (\phi^k b_{ki} + \nabla_i\psi)\hat{n} \tag{10}$$

$$\delta\hat{n} = \phi^k b_k^i + \nabla^i\psi \tag{11}$$

$$\delta g_{ij} = \nabla_i\phi_j + \nabla_j\phi_i - 2\psi b_{ij} \tag{12}$$

$$\delta\sqrt{g} = \sqrt{g}\left(\nabla_i\phi^i - 2H\psi\right) \tag{13}$$

$$\delta H = \psi(2H^2 - K) + \frac{1}{2}\nabla_i\nabla^i\psi + \phi^k\nabla_k H \tag{14}$$

Different parametrization used

Cylindrical parametrization with r as independent variable

Parametrization:

$$\vec{x}(r,\theta) = (r\cos\theta,\ r\sin\theta,\ z(r,\theta))$$

Partial derivatives:

$$\partial_r\vec{x} = (\cos\theta,\ \sin\theta,\ \partial_r z)$$
$$\partial_\theta\vec{x} = (-r\sin\theta,\ r\cos\theta,\ \partial_\theta z)$$

Metric tensor:

$$g = \begin{bmatrix} 1+(\partial_r z)^2 & \partial_r z\,\partial_\theta z \\ \partial_r z\,\partial_\theta z & r^2+(\partial_\theta z)^2 \end{bmatrix}$$

Unit normal vector:

$$\hat{n} = \left(\frac{\sin\theta\,\partial_\theta z - r\cos\theta\,\partial_r z}{\sqrt{(\partial_\theta z)^2 + r^2(1+(\partial_r z)^2)}},\ \frac{-\cos\theta\,\partial_\theta z - r\sin\theta\,\partial_r z}{\sqrt{(\partial_\theta z)^2 + r^2(1+(\partial_r z)^2)}},\ \frac{r}{\sqrt{(\partial_\theta z)^2 + r^2(1+(\partial_r z)^2)}}\right)$$

Inverse metric:

$$g^{-1} = \frac{1}{(\partial_\theta z)^2 + r^2(1+(\partial_r z)^2)}\begin{bmatrix} r^2+(\partial_\theta z)^2 & -\partial_r z\,\partial_\theta z \\ -\partial_r z\,\partial_\theta z & 1+(\partial_r z)^2 \end{bmatrix}$$

Second fundamental form:

$$\mathrm{II} = \begin{bmatrix} \dfrac{r\,\partial_r\partial_r z}{\sqrt{(\partial_\theta z)^2 + r^2(1+(\partial_r z)^2)}} & \dfrac{-\partial_\theta z + r\,\partial_r\partial_\theta z}{\sqrt{(\partial_\theta z)^2 + r^2(1+(\partial_r z)^2)}} \\ \dfrac{-\partial_\theta z + r\,\partial_r\partial_\theta z}{\sqrt{(\partial_\theta z)^2 + r^2(1+(\partial_r z)^2)}} & \dfrac{r(r\,\partial_r z + \partial_\theta^2 z)}{\sqrt{(\partial_\theta z)^2 + r^2(1+(\partial_r z)^2)}} \end{bmatrix}$$

Mean curvature :

$$H = \frac{r\,z_{\theta\theta}(1+z_r^2) + z_r\Big(r^2(1+z_r^2) + 2z_\theta(z_\theta - r z_{r\theta})\Big) + r(r^2+z_\theta^2)z_{rr}}{\Big(z_\theta^2 + r^2(1+z_r^2)\Big)^{3/2}}$$

Gaussian curvature:

$$K = \frac{-(z_\theta - r z_{r\theta})^2 + r^2(z_{\theta\theta} + r z_r)z_{rr}}{\left(z_\theta^2 + r^2(1+z_r^2)\right)^2}$$

Cylindrical parametrization with z as independent variable

Parametrization:

$$\vec{x}(t,z) = (\cos\theta \cdot r(z),\ \cos\theta \cdot r(z),\ z)$$

Partial derivatives:

$$\partial_z \vec{x} = (\cos\theta \cdot r'(z),\ \sin\theta \cdot r'(z),\ 1)$$
$$\partial_\theta \vec{x} = (-r(z)\sin\theta,\ r(z)\cos t,\ 0)$$

Metric tensor:

$$g = \begin{bmatrix} 1 + r'(z)^2 & 0 \\ 0 & r(z)^2 \end{bmatrix}$$

Unit normal vector:

$$\hat{n} = \left(-\frac{\cos\theta \cdot r(z)}{\sqrt{r(z)^2(1+r'(z)^2)}},\ -\frac{r(z)\sin\theta}{\sqrt{r(z)^2(1+r'(z)^2)}},\ \frac{r(z)r'(z)}{\sqrt{r(z)^2(1+r'(z)^2)}} \right)$$

Inverse metric:

$$g^{-1} = \begin{bmatrix} \frac{1}{1+r'(z)^2} & 0 \\ 0 & \frac{1}{r(z)^2} \end{bmatrix}$$

Second fundamental form:

$$\mathrm{II} = \begin{bmatrix} -\frac{r(z)r''(z)}{\sqrt{r(z)^2(1+r'(z)^2)}} & 0 \\ 0 & \frac{r(z)^2}{\sqrt{r(z)^2(1+r'(z)^2)}} \end{bmatrix}$$

Mean curvature:

$$H = \frac{(1 + r'(z)^2 - r(z)r''(z))}{r(z)\left((1+r'(z)^2)\right)^{3/2}}$$

Gaussian curvature:

$$K = -\frac{r''(z)}{r(z)(1+r'(z)^2)^2}$$

Derivation of the conservation equation

Let $\Sigma : \Omega \subset \mathbb{R}^2 \to \mathbb{R}^3$ be the reference configuration and $\Sigma'_t : \Omega' \subset \mathbb{R}^2 \to \mathbb{R}^3$ the time dependent configuration.
Define $\phi_t : S \to S'$, that is, the map that describes the motion of each point on the time dependent manifold.
The integral form of the conservation of a generic quantity $A : S' \times \mathbb{R} \to \mathbb{R}$ reads:

$$\frac{d}{dt}\int_{\phi_t(U)} A(X,t)d\sigma = 0,\ \forall U \subset S \tag{15}$$

Which can be written as:

$$\int_S \frac{d}{dt}(A(\phi_t(\mathbf{x}),t)J(\mathbf{x},t))\ dxdy = 0,\ \forall S \subset \Omega \Rightarrow \frac{d}{dt}(A(\phi_t(\mathbf{x}),t)J(\mathbf{x},t)) \tag{16}$$

Where $J(\mathbf{x},t)$ is the Jacobian of the transformation and it's equal to:

$$J(\mathbf{x},t) = \left|\frac{d(\Sigma'_t)^i}{d\Sigma^j}\right| = \sqrt{|g'(\phi_t(x),t)|}\left|\frac{d\phi_t^k(x)}{dx^l}\right|\sqrt{|g(x)|^{-1}} \tag{17}$$

Where chain rule has been used. The equation can be thus expanded:

$$\frac{d}{dt}(A(\phi_t(\mathbf{x}),t)J(\mathbf{x},t)) = \tag{18}$$

$$J(\mathbf{x},t)(\partial_t A(\phi_t(\mathbf{x}),t) + \partial_{X_i}A|_{X=\phi_t(\mathbf{x})}\partial_t\phi_t(\mathbf{x}))+ \tag{19}$$

$$+A(\phi_t(\mathbf{x}),t)(\frac{d}{dt}J(\mathbf{x},t)) \tag{20}$$

$$\frac{d}{dt}J(\mathbf{x},t) == \frac{d}{dt}\sqrt{g'(\phi_t(x),t)}\left(\left|\frac{d\phi_t^k(x)}{dx^l}\right|\sqrt{g(x)}\right)+ \tag{21}$$

$$+\sqrt{g'(\phi_t(x),t)}\frac{d}{dt}\left|\frac{d\phi_t^k(x)}{dx^l}\right|\sqrt{g(x)} \tag{22}$$

$$\tag{23}$$

where:

$$\frac{d}{dt}\sqrt{g'(\phi_t(x),t)} = \tag{24}$$

$$= \partial_\alpha\sqrt{g'(\phi_t(x),t)}\ v_\alpha + \partial_t\sqrt{g'(\phi_t(x),t)} \tag{25}$$

$$\partial_t\sqrt{g'(\phi_t(x),t)} = \frac{1}{2\sqrt{g'(\phi_t(x),t)}}(\mathrm{cof(g)})^{\alpha\beta}\partial_t g_{\alpha\beta} = \quad (26)$$

$$= \frac{\sqrt{g'(\phi_t(x),t)}}{2} g^{\alpha\beta}\partial_t(e^i_\alpha e^i_\beta) = \frac{\sqrt{g'(\phi_t(x),t)}}{2} 2 * g^{\alpha\beta}e^i_\alpha\partial_t(e^i_\beta) = \quad (27)$$

$$= \sqrt{g'(\phi_t(x),t)} * g^{\alpha\beta}e^i_\alpha\partial_\beta(v_\perp n^i) = -\sqrt{g'(\phi_t(x),t)} * g^{\alpha\beta}\partial_\beta(e^i_\alpha)v_\perp n^i = \quad (28)$$

$$-\sqrt{g'(\phi_t(x),t)} * b^\alpha_\alpha v_\perp \quad (29)$$

$$\frac{d}{dt}\left|\frac{\partial\phi^\alpha_t(x)}{\partial x^\beta}\right| = (\mathrm{cof})^{\alpha\beta}\frac{d}{dt}\frac{\partial\phi^\alpha_t(x)}{\partial x^\beta} = \quad (30)$$

$$= \left|\frac{\partial\phi^\alpha_t(x)}{\partial x^\beta}\right|(\frac{\partial x^\beta}{\partial\phi^\alpha_t(x)})\frac{\partial v^\alpha(\phi_t(x))}{\partial X^\gamma}\frac{\phi^\gamma_t(x)}{\partial x^\beta} = \left|\frac{\partial\phi^\alpha_t(x)}{\partial x^\beta}\right|\frac{\partial v^\gamma(\phi_t(x))}{\partial X^\gamma} \quad (31)$$

Where we have used the formula $d\det(A_{ij}) = \mathrm{cof}_{ij}dA^{ij}$.
The final result is:

$$\frac{d}{dt}J(\mathbf{x},t) = J(\mathbf{x},t)(\frac{1}{\sqrt{g'(\phi_t(x),t)}}v^\alpha\partial_\alpha\sqrt{g'(\phi_t(x),t)} - 2Hv_\perp + \partial_\alpha v^\alpha) \quad (32)$$

Substitution into the initial equation leads to:

$$\frac{d}{dt}(A(\phi_t(\mathbf{x}),t)J(\mathbf{x},t)) = \partial_t A + \nabla_\alpha(Av^a) - 2Hv_\perp = 0 \quad (33)$$

Variation of the Helfrich-Canhan's energy functional

In order to find the surface and line forces acting on the membrane, one has to evaluate to linear order the variation of the HC energy functional under small perturbations. Substitution of the variation of the quantities presented in appendix 4.3.1 gives:

$$\delta\mathcal{H}[z] = \delta\int_\Omega dS\left\{2\kappa H^2 + \kappa' K + \sigma\right\} = \quad (34)$$

$$= \int_\Omega dS\left\{\psi\left[4kH^3 - 2H\sigma - 4kHK\right] + \nabla_i\phi^i\left[2kH^2 + \sigma\right] + 2kH\nabla^i\nabla_i\psi\right\} \quad (35)$$

Integrating by parts two times the last term, one obtains:

$$2k \int dS(H\nabla^i \nabla_i \psi) = 2k \int dS(\psi \nabla_i \nabla^i H) + 2k \int dl(H n^i \nabla_i \psi - \psi n_i \nabla^i H) \tag{36}$$

The term $Hn^i \nabla_i \psi$ corresponds to a torque per unit length.
The final expression has the form:

$$\delta\mathcal{H}[z] = \int_\Omega dS \left[(4kH^3 - 2H\sigma - 4kHK + 2k\psi\nabla_i\nabla^i H)\psi\right] + \tag{37}$$

$$+ \int dl \left[2k(Hn^i\nabla_i\psi - \psi n_i \nabla^i H + n_i \phi^i (2kH^2 + \sigma))\right] \tag{38}$$

The total force acting on a line contour written in the real space will be:

$$\vec{F} = -\int dl \left[-2\kappa\hat{n}(n_i\nabla^i H) + n_i \vec{e}^{\,i}(2\kappa H^2 + \sigma)\right] \tag{39}$$

Analysis of solutions to the linear equation

In chapter 2 the solutions to the linear ODE have been presented. In this section we intend to derive those solutions.

$$(1 - \frac{r^2}{\ell^2})\, S(r) - rS'(r) + r^2\, S''(r) = 0 \quad \text{where} \quad S = \frac{w(r)}{r} \tag{40}$$

A first solution can be found in Taylor series form by substituting $S_\ell(r) = \sum_{i=0}^{+\infty} a_i r^i$ and finding a relation between the coefficients a_i. By doing so one obtains

$$a_i = \frac{\ell^{-2i}}{(2i!!)^2} \text{ if } i \text{ is odd} \tag{41}$$

$$a_i = 0 \text{ otherwise} \tag{42}$$

The second solution does not admit a Taylor series around $r = 0$, however, substituting $S_2(r) = S_1(r)S_*(r)$ one can reduce the degree of the equation and solve it directly. The final equation has the form:

$$S_*'' - S_*' \left(\frac{1}{r} - \frac{2S_1'}{S_1}\right) \tag{43}$$

Whose solution is:

$$S_2(r) = S_1(r) \int \frac{t}{S_1(t)^2} dt \tag{44}$$

Large r behavior

The large r behavior can be obtained through the change of variable $x = 1/r$ and considering the limit $x \to 0$.
After the substitution one obtains:

$$x^2 S'' + 3xS' + \left(1 + \frac{1}{\ell^2 x^2}\right) S = 0 \tag{45}$$

The point $x = 0$ is an irregular singular point, that is, the solution cannot be found in the form of a Taylor series (Frobenius method). However, asymptotic analysis can be applied to obtain the asymptotic behavior near $x = 0$. Assuming an asymptotic behavior of the form $S(x) = e^{K(x)}$ one finds the following differential equation for $K(x)$:

$$-\frac{1}{\ell^2 x^2} + 3xK' + x^2 (K')^2 + x^2 K'' = 0 \tag{46}$$

From the fact that one expect $K \sim x^{-\alpha}$, the equation can be transformed into an asymptotic relation valid for $x \to 0$, that is:

$$(K')^2 \sim \frac{1}{\ell^2 x^2} \Rightarrow K \sim \pm \frac{1}{\ell x} \tag{47}$$

The second order term can be obtained in the same way and it is equal to:

$$K_2(x) = -\frac{1}{2} \ln(x) \tag{48}$$

The final large r behavior can be obtained by substituting back $x = \frac{1}{r}$. The result is:

$$S_{\pm}(r) \sim e^{\pm \frac{r}{\ell}} \sqrt{r} \left(c_0 + \frac{c_1}{r} + ..\right) \tag{49}$$

To leading order:

$$S_{\pm}(r) \sim e^{\pm \frac{r}{\ell}} \sqrt{r} \tag{50}$$

Large gradient expansion

In the second chapter we performed a large gradient expansion, by considering $r = r(z)$. If one consider $r(z) = r_0 + u(z)$, with $u(z) << r_0$, then the previous

quantities become to linear order:

$$\sqrt{|g|} = r_0 + u + o(u) \tag{51}$$

$$H \sim \frac{1}{r_0} - u'' - \frac{u}{r_0^2} + o(u) \tag{52}$$

$$K \sim -\frac{u''}{r_0} \tag{53}$$

$$g^{zz} \sim 1 \tag{54}$$

$$b_z^z \sim b_{zz} \sim -u'' \tag{55}$$

$$\tag{56}$$

The equation will be:

$$\frac{2 - ar_0^2}{r_0^3} - \left(\frac{6 - ar_0^2}{r_0^4}\right) u - \left(\frac{5 - ar_0^2}{r_0^2}\right)\ u''(z) - u''''(z) = 0 \tag{57}$$

Given that $u << r_0$, necessarily $r_0 = \sqrt{\frac{2}{a}}$, from which one finds:

$$a^2 u + \frac{3a}{2} u'' + u'''' = 0 \tag{58}$$

The characteristic polynomial has 4 complex roots that are:

$$\lambda = \pm\sqrt{a}e^{i\theta}, \pm\sqrt{a}e^{-i\theta} \tag{59}$$

The general solution will have the form:

$$u = c_1 e^{-\Re\{\lambda\}t} \cos(\Im\{\lambda\}t + \phi_1) + c_2 e^{\Re\{\lambda\}t} \cos(\Im\{\lambda\}t + \phi_2) \tag{60}$$

That is, any deviation from r_0 will exponentially decay in an oscillatory way.

Bibliografia

[1] Imre Derényi, Frank Jülicher e Jacques Prost. «Formation and Interaction of Membrane Tubes». In: *Physical Review Letters* 88.23 (mag. 2002), p. 238101. ISSN: 0031-9007, 1079-7114. DOI: 10.1103/PhysRevLett.88.238101. (Visitato il giorno 14/06/2025) (cit. alle pp. 1, 22).

[2] Marino Arroyo e Antonio DeSimone. «Relaxation Dynamics of Fluid Membranes». In: *Physical Review E* 79.3 (mar. 2009), p. 031915. ISSN: 1539-3755, 1550-2376. DOI: 10.1103/PhysRevE.79.031915. (Visitato il giorno 14/06/2025) (cit. a p. 4).

[3] Jerrold E. Marsden e Thomas J. R. Hughes. *Mathematical Foundations of Elasticity*. Prentice-Hall Civil Engineering and Engineering Mechanics Series. Englewood Cliffs, NJ: Prentice-Hall, 1983. ISBN: 978-0-13-561076-3 (cit. a p. 4).

[4] Dennis Wörthmüller, Gaetano Ferraro, Pierre Sens e Michele Castellana. «IRENE: A fluId layeR finitE-elemeNt softwarE». In: (2025). DOI: 10.48550/ARXIV.2506.17827. (Visitato il giorno 12/07/2025) (cit. alle pp. 6, 12).

[5] Balázs Fábián, Ilpo Vattulainen e Matti Javanainen. «Protein Crowding and Cholesterol Increase Cell Membrane Viscosity in a Temperature Dependent Manner». In: *Journal of Chemical Theory and Computation* 19.9 (mag. 2023), pp. 2630–2643. ISSN: 1549-9618, 1549-9626. DOI: 10.1021/acs.jctc.3c00060. (Visitato il giorno 12/07/2025) (cit. a p. 6).

[6] Bruno Pontes et al. «Membrane Elastic Properties and Cell Function». In: *PLoS ONE* 8.7 (lug. 2013). A cura di Stefan Ft. Weiss, e67708. ISSN: 1932-6203. DOI: 10.1371/journal.pone.0067708. (Visitato il giorno 12/07/2025) (cit. a p. 6).

[7] Michael M Kozlov, Felix Campelo, Nicole Liska, Leonid V Chernomordik, Siewert J Marrink e Harvey T McMahon. «Mechanisms Shaping Cell Membranes». In: *Current Opinion in Cell Biology* 29 (ago. 2014), pp. 53–60. ISSN: 09550674. DOI: 10.1016/j.ceb.2014.03.006. (Visitato il giorno 14/06/2025) (cit. a p. 16).

[8] Carl M. Bender e Steven A. Orszag. «Advanced Mathematical Methods for Scientists and Engineers. 1: Asymptotic Methods and Perturbation Theory». In: Nachdr. New York, NY: Springer, 2009. ISBN: 978-0-387-98931-0 (cit. a p. 16).

[9] Robijn Bruinsma e Philip Pincus. «Protein Aggregation in Membranes». In: *Current Opinion in Solid State and Materials Science* 1.3 (giu. 1996), pp. 401–406. ISSN: 1359-0286. DOI: 10.1016/s1359-0286(96)80032-5. (Visitato il giorno 14/07/2025) (cit. alle pp. 25, 34).

[10] Lev Davidovič Landau, Evgenij M. Lifšic e Lev Davidovič Landau. *Fluid Mechanics*. Trad. da J. B. Sykes e William Hill Reid. Second English edition, revised. Course of Theoretical Physics volume 6. Amsterdam Boston Heidelberg: Elsevier, Butterworth-Heinemann, 1987. ISBN: 978-0-08-057073-0 (cit. a p. 30).

[11] John Happel e Howard Brenner. *Low Reynolds Number Hydrodynamics: With Special Applications to Particulate Media*. Mechanics of Fluids and Transport Processes. Dordrecht: Springer Netherlands, 1983. ISBN: 978-90-247-2877-0 978-94-009-8352-6. DOI: 10.1007/978-94-009-8352-6. (Visitato il giorno 11/07/2025) (cit. a p. 32).

[12] Sami C. Al-Izzi, Pierre Sens e Matthew S. Turner. «Shear-Driven Instabilities of Membrane Tubes and Dynamin-Induced Scission». In: *Physical Review Letters* 125.1 (lug. 2020), p. 018101. ISSN: 0031-9007, 1079-7114. DOI: 10.1103/PhysRevLett.125.018101. arXiv: 1810.05862 [physics]. (Visitato il giorno 14/06/2025).

[13] Anne-Florence Bitbol, Doru Constantin e Jean-Baptiste Fournier. «Membrane-Mediated Interactions». In: (2019). DOI: 10.48550/ARXIV.1903.05712. (Visitato il giorno 14/07/2025).

[14] W Helfrich. «Elastic Properties of Lipid Bilayers: Theory and Possible Experiments». In: *Zeitschrift für Naturforschung C* 28.11-12 (dic. 1973), pp. 693–703. ISSN: 1865-7125, 0939-5075. DOI: 10.1515/znc-1973-11-1209. (Visitato il giorno 14/06/2025).

[15] Lev Davidovič Landau, Evgenij M. Lifšic, Lev Davidovič Landau e Lev Davidovič Landau. *Theory of Elasticity*. 3. Engl. ed., rev. and enlarged, [Nachdr.] Course of Theoretical Physics / L. D. Landau and E. M. Lifshitz 7. Amsterdam Heidelberg: Elsevier, Butterworth-Heinemann, 2009. ISBN: 978-0-7506-2633-0.

[16] Hans Petter Langtangen e Anders Logg. *Solving PDEs in Python: The FEniCS Tutorial I*. 1st ed. 2016. Simula SpringerBriefs on Computing 3. Cham: Springer International Publishing : Imprint: Springer, 2016. ISBN: 978-3-319-52462-7. DOI: 10.1007/978-3-319-52462-7.

[17] Manqing Li, Xiumei Xing, Jianhui Yuan e Zhuoying Zeng. «Research Progress on the Regulatory Role of Cell Membrane Surface Tension in Cell Behavior». In: *Heliyon* 10.9 (mag. 2024), e29923. ISSN: 2405-8440. DOI: 10.1016/j.heliyon.2024.e29923. (Visitato il giorno 12/07/2025).

[18] J. N. Reddy. *Introduction to the Finite Element Method, Third Edition*. 3rd edition. New York, N.Y: McGraw-Hill Education, 2006. ISBN: 978-0-07-246685-0 978-0-07-124473-2.